Journal of Environmental Management 236 (2019) 519–533

Contents lists available at ScienceDirect

Journal of Environmental Management

journal homepage: www.elsevier.com/locate/jenvman

Research article

Photocatalytic degradation of local dyeing wastewater by iodine-phosphorus co-doped tungsten trioxide nanocomposites under natural sunlight irradiation

J.O. Tijani[a,c,*], O. Ugochukwu[a,c], L.A. Fadipe[a], M.T. Bankole[a,c], A.S. Abdulkareem[b,c], W.D. Roos[d]

[a] Department of Chemistry, Federal University of Technology, PMB. 65, Minna, Niger State, Nigeria
[b] Department of Chemical Engineering, Federal University of Technology, PMB.65, Minna, Niger State, Nigeria
[c] Nanotechnology Research Group, Centre for Genetic Engineering and Biotechnology (CGEB), Federal University of Technology, P.M.B 65, Bosso, Minna, Niger State, Nigeria
[d] Department of Physics, University of the Free State, P.O. Box 339, ZA-9300 Bloemfontein, South Africa

ARTICLE INFO

Keywords:
Green synthesis
Tungsten trioxide
Spondias mombin
Co-doping
Iodine
Phosphorus monoclinic phase
Photocatalysis

ABSTRACT

In the present work, one-step green synthesis of WO_3 based on the interaction of ammonium paratungstate and *Spondias mombin leaves* extract is reported. Different concentrations of iodine and phosphorus in the range of (2%, 5% and 10%) were firstly incorporated into the prepared WO_3 nanoparticles to obtain Iodine doped and Phosphorus doped WO_3 nanoparticles respectively. Subsequently, iodine and phosphorus co-doped WO_3 nanocomposites was prepared using a wet impregnation method followed by calcination at high temperature. The nanomaterials were characterized by HRSEM, HRTEM, BET, UV–Visible, EDS, XRD and XPS. The photo-oxidation of dyeing wastewater by the synthesized WO_3 nanomaterials were tested and assessed using Total organic carbon (TOC) and Chemical oxygen demand (COD) as indicator parameters. XRD and HRSEM analysis demonstrated the formation of only monoclinic phase of WO_3 irrespective of the dopants. The UV–Visible diffuse reflectance spectroscopy showed the band gap energy of 2.61 eV for undoped WO_3 and 2.02 eV for I-P co-doped WO_3 nanocomposites. The surface area of I-P co-doped WO_3 (416.18 m^2/g) was higher than the undoped WO_3 (352.49 m^2/g). The XPS demonstrated interstitial and substitution of oxygen (O^{2-}) vacancies in WO_3 by I^- and P^{3+} and formed I-P-$WO_{(3-x)}$. The I-P co-doped WO_3 exhibited higher catalytic activities (93.4% TOC, 95.1% COD) than the undoped (54.9% TOC, 79.2% COD) due to the synergistic effects between the two dopants. The experimental data better fitted to pseudo-second order than first order and pseudo-first order model. This study demonstrated the enhanced photocatalytic performance of I-P co-doped WO_3 nanocomposites under sunlight.

1. Introduction

Water is an essential natural resource required for human survival and sustainability. However, increase in human population, industrial expansion, urbanization, poor agricultural practices coupled with flooding activities have led to over exploitation and contamination of this scarce resource (Gupta et al., 2015). The natural and anthropogenic activities disrupted the balance between the usage and natural purification processes leading to a shortage of potable water (Baruah et al., 2012; UN, 2017). Furthermore, approximately 2 million tons of sewage from industrial and agricultural wastes are discharged into the world water bodies (WWAP, 2015). Moreover, local dyeing industries use and discharge large volumes of water containing complex non-biodegradable recalcitrant organic and inorganic chemicals into the environment. The local dyeing wastewater have an offensive odour, highly coloured, low pH, and exposure to such wastewater can cause several diseases among which are cancer, skin irritation to mention but a few (Ghaly et al., 2014). In developing countries like Nigeria, indiscriminate discharge of untreated solid and liquid waste is still a common current practice especially among local dyeing firms (Uwidia, 2011; Uwidia and Ademoroti, 2012). For instance, in Kano State, an average of over 40 drums per day equivalent of 8320 L of local dyeing effluent are directly released untreated into the water bodies. This action is considered as one of the biggest threats to human and aquatic species due to the presence of highly recalcitrant and toxic aromatic dye molecules (Ghaly et al., 2014; Ntuli et al., 2009).

Several physical, chemical and biological methods have been utilized to treat local dyeing wastewater (Neppolian et al., 2002).

* Corresponding author. Department of Chemistry, Federal University of Technology, PMB. 65, Minna, Niger State, Nigeria.
E-mail address: jimohtijani@futminna.edu.ng (J.O. Tijani).

https://doi.org/10.1016/j.jenvman.2019.02.027
Received 25 August 2018; Received in revised form 12 January 2019; Accepted 6 February 2019

However, restrictions in terms of execution, efficiency, and cost remain a challenge militating against widely acceptability of some of these techniques (Ghaly et al., 2014; Sin et al., 2012). In view of the highlighted shortcomings, advanced oxidation technologies (AOTs) based on the utilization of highly oxidizing species such as hydroxyl radicals, hydrogen peroxide, ozone has been widely recognized for the decomposition of toxic organic molecules into carbon dioxide and water (Dalrymple et al., 2007). Among several promising AOTs, heterogeneous photocatalysis involving oxidation and reduction reaction on semiconductor surfaces based on the absorption of ultraviolet or visible light radiation has been widely investigated due to its multitude of applications in the area of solar cells and environmental remediation of toxic pollutants in water and air (Braslavsky, 2007; Mu et al., 2015).

Several semiconductor metal oxides namely (TiO_2, ZnO, MoO_3, ZrO_2, WO_3, α-Fe_2O_3, SnO_2, $SrTiO_3$, In_2O_3) and metal chalcogenides (ZnS, CdS, CdSe, WS_2, MoS_2) have been utilized as photocatalysts to decompose recalcitrant organic pollutants in wastewater. Specifically, tungsten trioxide (WO_3) nanoparticles has emerged as a suitable candidate due to their smaller band gap, electrochromic, photochromic and gasochromic properties (Chang et al.,2011) as well as diverse applications as photocatalysts (Liu et al., 2007), photoluminescent materials (Supothina et al., 2013), anti-glare mirrors, sensors (Hariharan et al., 2011) amongst others. In addition, WO_3 is an n-type, inorganic and functional semiconductor material with a band gap of between 2.4 and 2.8 eV and have the tendencies to absorb more solar energy and produce a high photocurrent than TiO_2 (Rao and Hussain, 2011). On the other hand, WO_3 has lower light energy conversion rate and lower conduction band (CB) edge potential (+ 0.3–0.5 V vs. NHE) and as such cannot reduce dioxygen in the aqueous medium which affect its efficiency (Ng et al., 2013). More so, there is substantial accumulation and recombination of the photo-excited electrons on the surface of the catalyst and as such responsible for the low photocatalytic efficiencies of the catalyst under sunlight (Seyama et al., 2012).

The preparation of WO_3 nanoparticles have been achieved by various methods such as sol gel (Li et al., 2014); acidification (Supothina et al., 2007); chemical vapour deposition (Mahan et al., 2005); hydrothermal (Komaba et al., 2000); electrodeposition (Bhyuiyan et al., 2006); thermal evaporation (Liu et al., 2003); electrospinning (Nguyen et al., 2011); and pulsed laser deposition (Fonzo et al., 2006) amongst others. These conventional physical and chemical methods require complicated procedure, generate toxic bye products, time consuming and costly (Chauhan et al., 2012). Recently, there has been growing interest in the synthesis of nanoparticles through environmentally benign protocol that utilizes plant extracts or microbes than conventional physical and chemical methods. This method is considered more economical, energy and time saving and eco-friendly and do not require complex procedures and plant materials often act as a reducing, stabilizing and capping agent (Li et al., 2011). This green synthesis method has been used in the production of silver, gold, palladium and many other metal nanoparticles and the nature of the plant extract, the concentration of secondary metabolites, the concentration of the metal salt, the pH, have been reported to influence the rate of production of the nanoparticles, their quantity and other characteristics (Dwivedi and Gopal, 2010; Li et al., 2011).

Furthermore, researchers have employed different strategies to improve the photocatalytic activity of WO_3 in the visible light region which include: surface modification and control of morphology and particle size, preparation of composite materials, transition/noble metal doping, non-metal doping, metal doping, metal deposition and surface sensitization to mention but a few (Asim et al., 2013). Research on doping of WO_3 with metals or non-metals such as Zn, Ti, Ag, Fe, Mg, Mo, S, N, C, and P designed to extend the photocatalytic performance of a semiconductor lower energy conversion has spanned several decades. The doping mechanism enhanced the net separation of photo-generated charges and enable the conversion of a wide visible-light component of about 43% in the solar spectrum compared to the narrow ultraviolet component of 5% (Ibhadon and Fitzpatrick, 2013). Doping of WO_3 with metalloids, lanthanide, biogenic elements or transition metals have been found to favoured band gap reduction (Sathishkumar et al., 2013); increased impurity energy levels (Cao et al., 2013); creation of oxygen vacancies (Wu et al., 2010); trapping of photoelectrons (Barakat et al., 2013); charge compensation (Jin and Liu, 2016) and enhanced photoactivity response to visible light. The photocatalytic properties of the following doped nanocomposites: Fe/WO_3, Pt/WO_3, S/WO_3, I/WO_3, F/WO_3, N-TiO_2/WO_3 prepared using template, hydrothermal, sol-gel, co-precipitation methods under ultra-violet and visible light have been reported in the literature (Aminian, 2009; Song et al., 2014; Wicaksana et al., 2014; Zhang et al., 2012). Conversely, it was demonstrated that mono-doped WO_3 nanoparticles usually exhibited low photocatalytic activity primarily due to the promotion of the charge carrier recombination.

Actually synthesis of WO_3 nanoparticles by physical and chemical methods have been widely reported however information on the green synthesis of WO_3 involving tungsten precursor and plant extract is scarce in the literature. In addition, there is little or no information on the green synthesis and photocatalytic activity of phosphorus doped WO_3 nanoparticles under natural sunlight irradiation. In this present work, green synthesis of WO_3 nanoparticles using *Spondias mombin* aqueous leaf extract was explored. The synthesized WO_3 nanoparticles was simultaneously doped and co-doped with phosphorus and iodine. The synergistic effect of doping with I_2 and P could help suppress the recombination of photo-generated electron-hole pairs by inducing a local inner built-in electric field and eliminating the deep impurity energy of mono-doped P or I_2. Furthermore, the photon absorption could be extended in the visible region, due to overlapping of impurity energy band with the top of the valence band or bottom of the conduction band, and consequently improve the photocatalytic activity of I-P-WO_3 on local dyeing wastewater. In the present work, the photocatalytic degradation of the local dyeing wastewater under natural sunlight irradiation by pure, mono doped and co-doped I_2-P-WO_3 nanocomposites were investigated. The structural, morphological, surface chemical oxidation states, band gap energy of the prepared nanomaterials were examined.

2. Materials and methods

All chemicals and reagent such as ammonium iodide, ammonium hydroxide, ammonium paratungstate, sodium hydroxide, ammonium hydroxide tetra oxophosphate (VI) acid, nitric acid used in this study are of analytical grade and were used without any further purification.

2.1. Sample collection and pre-treatment

The local dyeing wastewater was collected from Kofar Mata dyeing pits in Kano, Nigeria and stored in clean polythene bottles prior to analysis. The bottles were pre-washed with 10% nitric acid and thoroughly rinsed with de-ionized water, and the wastewater was transferred to the laboratory and stored at 4 °C in the refrigerator to avoid any change in its characteristics. Fresh *Spondias mombin* (Plum Hog) leaves were randomly collected from Bida, Niger State. The leaves were washed and sun-dried in the open air for a week, and finally ground to fine powder using a mechanical blender.

2.2. Extraction of Spondias mombin plant extract

A known weight (50 g) of the powdered leaves of *Spondias mombin* were weighed into 500 cm^3 of methanol in a reflux flask and refluxed for 2 h. The extract was filtered using muslin cloth and subsequently evaporated on a rotary evaporator. The semi-dry extract was weighed, placed in a sterile bottle and stored in a refrigerator until further analysis.

2.3. Green synthesis of WO_3 nanoparticles

A known volume (10 cm^3) of *Spondias mombin* leaves extract was added drop by drop to 100 cm^3 of 0.06 M ammonium paratungstate solution in a 250 cm^3 conical flask and the mixture was gently heated at 120 °C under continuous stirring at 150 rpm for 1 h. Subsequently, 10% HNO_3 or 0.5 M NH_4OH was added drop wise to adjust the pH value to 1 and the solution was further stirred for 30 min. A change in colour from rusty brown to yellow accompanied with the formation of precipitates and was allowed to age for 24 h after which the precipitate was separated from the aqueous extract, first by decantation, and then followed by several washing with deionized water to remove any residual aqueous extract or impurities. The resultant precipitate was dried at 80 °C in a moisture extractor for 6 h and thereafter calcined at 550 °C in a furnace under air for 2 h.

2.4. Synthesis of iodine doped WO_3 nanoparticles

Iodine doped WO_3 nanoparticles (I-WO_3) was prepared by a combination of green hydrolysis and precipitation method described as follow: 10 cm^3 of *Spondias mombin* extract was measured and mixed with 70 cm^3 of 0.06 M of ammonium paratungstate in a 250 cm^3 conical flask. Thereafter; 20 cm^3 of 2% of ammonium iodide was added slow-wise to form a homogenous solution and the reaction mixture was vigorously stirred at 150 rpm for 1 h. The obtained precipitate was aged for 24 h, and then washed severally with distilled water to remove unreacted residue. The precipitate was oven dried at 80 °C for 6 h followed by calcination in the furnace at 550 °C for 2 h. The above procedure was repeated for 5 and 10% dopant concentration.

2.5. Synthesis of phosphorus WO_3 nanoparticles

The procedure reported for Iodine doped WO_3 was repeated to prepare Phosphorus doped WO_3 nanoparticles (P-WO_3). 2%, 5 and 10% ammonium phosphate was prepared and used as a dopant in a similar manner with ammonium iodide under the same experimental conditions.

2.6. Synthesis of iodine-phosphorus co-doped nanocomposites

The iodine and phosphorus co-doped WO_3 nanocomposites (I-P-WO_3) was synthesized as follows; firstly, 20 cm^3 of *Spondias mombin* extract was measured and mixing with 100 cm^3 of 0.06 M ammonium paratungstate in a 250 cm^3 conical flask. This was followed by addition of 2% ammonium iodide and ammonium phosphate and thereafter stirred on a magnetic stirrer at 150 rpm for 1 h to form a homogenous solution. The precipitate obtained was left to age for 24 h and the supernatants decanted and the precipitate was washed several times with distilled water to remove excess plant extract and other impurities. The resultant precipitate was oven-dried at 80 °C for 6 h and calcined in the furnace at 550 °C for 2 h.

2.7. Characterization of the nanomaterials

The absorption or wavelength of absorption of the synthesized nanomaterials was determined using Shimadzu UV–Visible spectrophotometer 1800. The surface morphology and elemental analysis of the co-doped and undoped WO_3 were examined by High Resolution Scanning Electron Microscope (HRSEM) model Ziess Auriga coupled Energy Dispersive Spectroscopy (EDS). The microstructure and polycrystalline nature of the nanomaterial was investigated by High Resolution Transmission Electron Microscope (HRTEM). The phase structure and crystalline particle size was determined using X-ray Diffractometer Bruker AXS D8 with Cu-kα radiation. The surface area of the synthesized materials using BET (Brunauer Emmett Teller) model NOVA 2400e while the surface properties such as orbital type and oxidation states of the prepared nanomaterials were evaluated by X-ray Photoelectron Spectrophotometer (XPS) PHI 5400 with an X-ray source of Mg Kα non-monochromatic in which a photoelectron take-off angle for all measurements was 45°. Survey scan analyses were carried out with a pass energy of 178.95 eV in steps of 0.5 eV and scan rate of 5 eV/s with no charge.

2.8. Physico-chemical characterization of local dyeing wastewater

The physico-chemical assessment of the local dyeing wastewater was carried out before and after treatment with the synthesized WO_3 nanocomposite under sunlight irradiation. The collected samples were analyzed for pH, conductivity, turbidity, chemical oxygen demand (COD), total dissolved solids (TDS), and total organic carbon (TOC), The parameters were analyzed according to establish standard method described by American Public Health Association, (APHA, 2012). The determination of TOC of the dyeing wastewater were performed using a Total Organic Carbon Analyzer TOC – Apollo 9000 manufactured by Tekmar Instruments. In the first instance, the carbon content in the sample (50 cm^3) was converted to CO_2 in the combustion furnace and thereafter carrier gas was flown to the combustion tube to carry the combustion products to an electronic dehumidifier, where the gas was cooled and dehydrated. A non-dispersive infrared detection (NDIR) generated a non-linear signal that is proportional to the instantaneous concentration of CO_2 in carrier gas. That signal was then plotted against the samples analysis time. The peak area was proportional to the TC concentration of the sample (APHA, 2012). The dichromate method described by American Public Health Association was used for the determination of COD. The amount of dichromate is determined by direct titration using Ferrous Ammonium Sulfate (FAS) as the titrant and ferroin (1, 10 phenanthroline ferrous sulfate) as the indicator (APHA, 2012).

2.9. Photocatalytic studies

Prior to photocatalytic studies, 1 g of the nanomaterials was added to 0.1 L of the local dyeing wastewater in a 0.25 L conical flask. The mixture was agitated on a magnetic stirrer at 150 rpm in the darkness without sunlight for 6 h. Sampling was done at regular interval of 1 h and subsequently analyzed for TOC and COD respectively. This was done to establish the adsorption potential of the synthesized nanomaterials. Again, 0.1 L of the local dyeing wastewater was measured into 0.25 L conical flask and then exposed to sunlight alone and agitated on a magnetic stirrer at 150 rpm for 6 h. Sampling was done periodically at time interval and analyzed for TOC and COD. This was done to show that % removal or mineralization of the organic dyes in the local dyeing wastewater at ambient temperature was due to the photolysis alone and not photocatalysis or adsorption behaviour of the nanomaterials. The photocatalytic experiments were performed using an improvised 0.5 L photo-reactor filled with 0.1 L of the local dyeing wastewater containing 1 g of WO_3 nanoparticles. Thereafter, in order to ensure that the adsorption–desorption equilibrium of the dye molecules on the catalyst surface had been reached; the mixture was kept under magnetic stirring in the dark for 60 min prior to exposure to sunlight. The whole set-up was then placed under sunlight with average intensity of $1.75 \times 10^{\wedge 5}$ Lux units or 252.92 W/m^2 at ambient temperature of 35 °C without adjusting the pH of the wastewater. Furthermore, the mixture was stirred continuously on a magnetic stirrer at 150 rpm and the mineralization of the dye molecule in the wastewater was monitored for 6 h. Sampling of aliquots was done from the reactor at various irradiation time intervals (0 h, 1 h, 2 h, 3 h, 4 h, 5 h and 6 h) and centrifuged for 10 min at 12,000 rpm to remove the residual catalyst. This procedure was then repeated for P-WO_3, I-WO_3 and I-P-WO_3 following the same experimental conditions. The photocatalytic degradation of the local dyeing wastewater by undoped, mono and co-doped WO_3 nanoparticles under sunlight irradiation source was measured using TOC and COD as

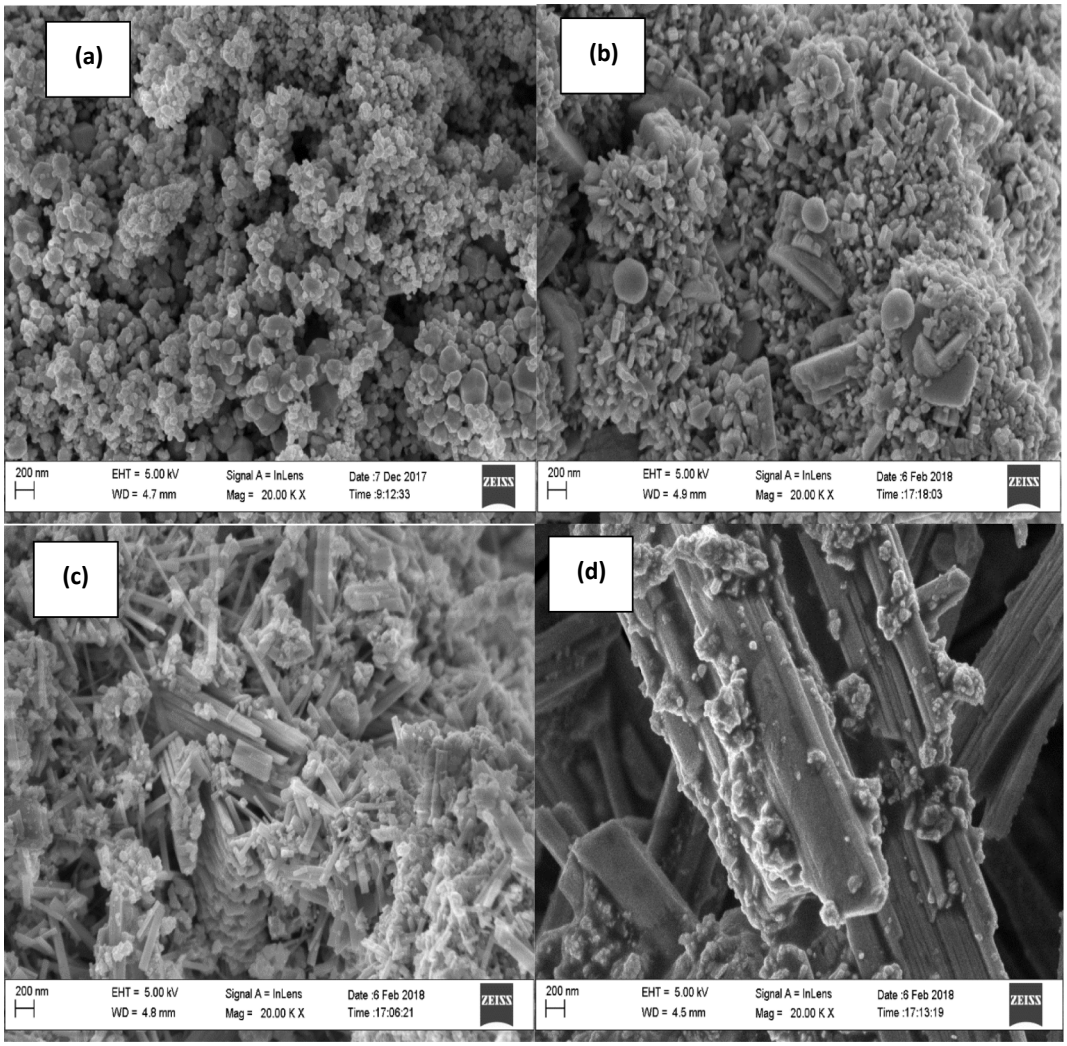

Fig. 1. HRSEM images for (a) undoped WO_3 (b) 2% I doped WO_3, (c) 5% I doped WO_3, (d) 10% I doped WO_3.

indicator parameters. The percentage of TOC was calculated using the equation (1)

$$Efficiency\ (\%) = \frac{TOC_O - TOC_1}{TOC_O} \times 100 \quad (1)$$

While th\e percentage COD removal was estimated using equation (2)

$$Efficiency\ (\%) = \frac{COD_o - COD_1}{COD_O} \times 100 \quad (2)$$

3. Results and discussion

3.1. HRSEM analysis for I-doped WO_3, P-doped WO_3 and I-P-doped WO_3 nanocomposites

The HRSEM images of the prepared nanomaterials are shown in Figs. 1–3. The HRSEM micrographs of the I-doped WO_3 (Fig. 1 (a) and (b)) revealed spherical morphology with average diameter of 1.1 and 1.5 nm for undoped and 2% I-doped WO_3 respectively. A close look at Fig. 1 (b) showed a greater proportion of the spherical morphology as well as small number of rod-like network. This implies that 2% iodine loading did not cause significant distortion and phase change of WO_3 nanoparticles. With 5% loading of iodine on WO_3, transformation of the spherical morphology to rod-like morphology was observed. While 10% iodine loading had a more compacted and well aligned rod-like shape. Similar morphological transformation of WO_3 nanoparticles from spherical to elongated rod-like morphology was observed as the concentration of phosphorus increased from 2% to 10% as shown in Fig. 2. Comparatively, short and nearly uniform rod-like shapes were observed for I-WO_3, while in the case of P-WO_3, long and thick bamboo-like morphology were formed. In Fig. 3, for I-P co-doped WO_3, complete morphological transformation from spherical symmetry to rod-like structure was observed. The difference may be attributed to the nature of the dopant vis-a-viz, ionic size and atomic weight. It appears that both I^- and P^{+3} dopant acted as a structure directing agents due to formation of a less compacted rod and hexagonal nanostructures relative to spherical and cubic structure observed for the undoped WO_3. This finding however differ from the outcome of Wicaksana et al. (2014) who used sulfate as a directing agent on WO_3 morphology and produced randomly orientated aligned nanorods. However, in this study, iodine and phosphorus doped WO_3 nanocomposites clearly exhibited uncapped mechanism owing to the formation of well aligned rod-like morphologies. The formation of the nanorods to align parallel in the case of WO_3 doped with 10% (iodine or phosphorus) may be explained in terms of high lateral capillary forces causing side-by-side alignment rather than end-to-end (Wicaksana et al., 2014). The formation of bamboo-like or nanorod bundles in the case of I-P co-doped WO_3 can be explained in terms of the oriented attachment due to the existence of synergetic effect which helped in the reduction of the surface energy of the system (Wang et al., 2009).

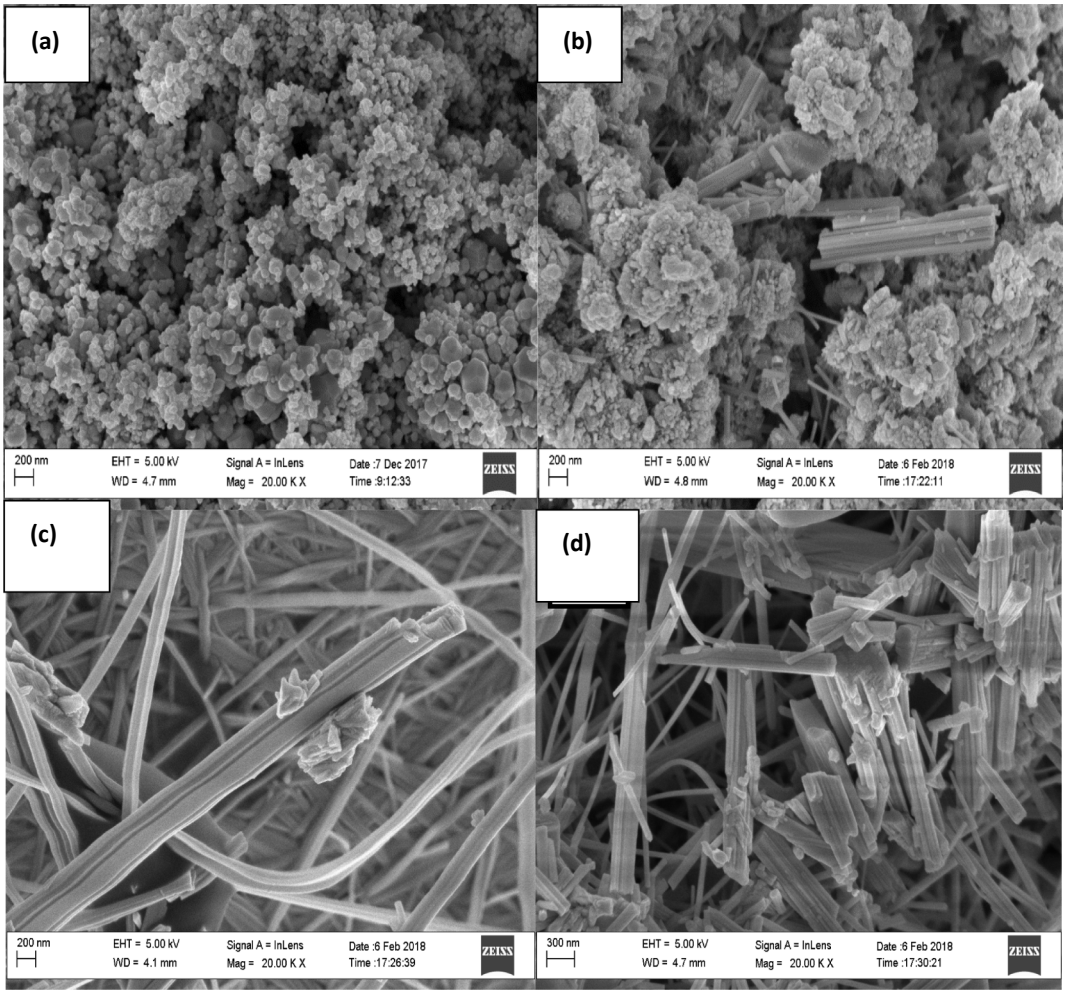

Fig. 2. HRESM images (a) undoped WO_3 (b) 2% P doped WO_3, (c) 5% P doped WO_3, (d) 10% P doped WO_3.

3.2. HRTEM-SAED analysis for I-doped WO_3, P-doped WO_3, and I-P co-doped WO_3 nanocomposites

Figs. 4 and 5 show HRTEM micrographs of WO_3 nanoparticles doped with (2–10%) of iodine and phosphorus with their corresponding SAED pattern at low and high magnification respectively. While Fig. 6 depicts the HRTEM/SAED images of iodine and phosphorus co-doped WO_3 nanocomposites.

In the case of 2% doped I-WO_3 (Fig. 4(1a, 1b)) and 2% doped P-WO_3 (Fig. 5 (2a, 2b)), mixture of long thick and thin rod-like nanostructures with average length of approximately 13.0 and 15.8 nm respectively were observed. However, as concentration of the dopants increased

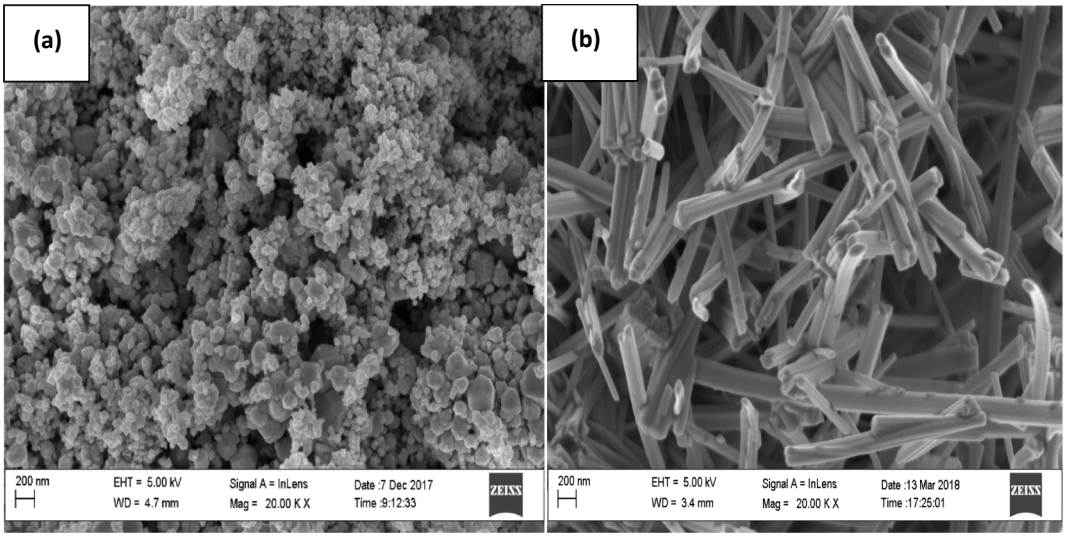

Fig. 3. HRESM images for (a) undoped WO_3 (b) 2% P &I co-doped WO_3.

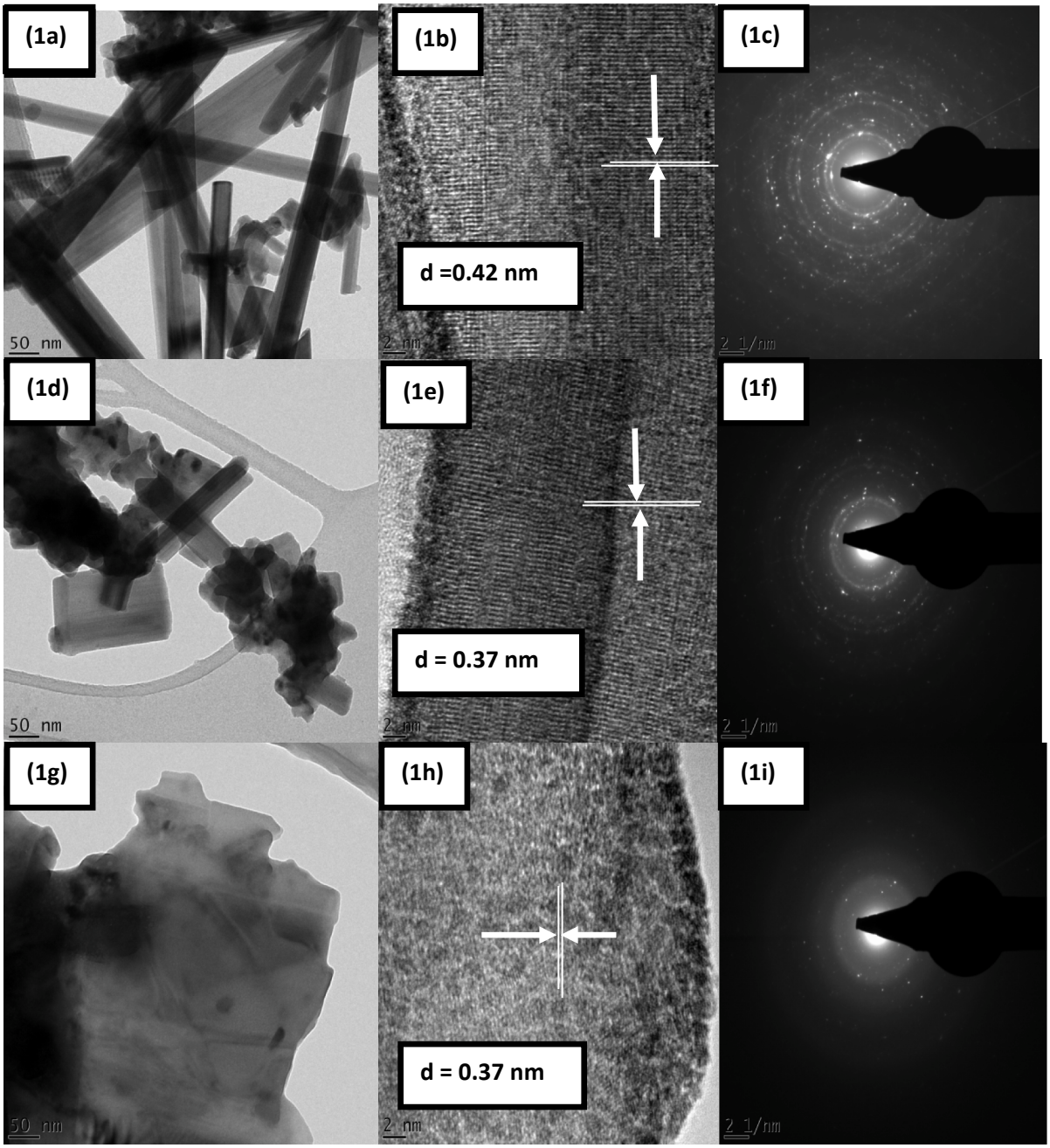

Fig. 4. (1a) & (1b) HRTEM images for 2% I-WO_3, (1c) SAED images for 2% I-WO_3. (1d) & (1e) HRTEM images for 5% I-WO_3, (1f) SAED images for 5% I-WO_3. (1g) and (2h) HRTEM images for 10% I-WO_3, (1i) SAED images for 10% I-WO_3.

from 5% to 10% (see Figs. 4 and 5), the average length of the rod – shaped morphology of the I-WO_3 nanoparticles reduced to 11.0 nm. Similarly, structures with average length of 15.0 nm was observed for P-WO_3. Although, the rods were partially agglomerated but no sign of the formation of hard agglomerates or neck formation. In spite of the formation of spherical and rod shaped WO_3 nanoparticles, their crystal structures still remained the same. The selected area electron diffraction (SAED) patterns and low magnification HRTEM images of the WO_3 nanoparticles shown in Figs. 4 and 5 revealed the presence of bright spots and lattice fringes which clearly indicates relatively high crystallinity for I, P and I-P co-doped WO_3 nanocomposites for both the spherical and rod-like shaped WO_3 structures. The spacing of the lattice fringes (d) was found to be about 0.37 nm for I-WO_3, 0.33 nm for P-WO_3 and 0.31 for I-P-WO_3 nanocomposites which corresponds to the [002] crystal planes and further confirmed that the rod prefers to grow along [002] direction. In addition, As the concentration of I increases on the lattice layer of WO_3, it was noticed that the clear lattice planes become slightly distorted, suggesting inhibition of the WO_3 nanoparticles along the growth direction of [002]. This further confirmed that immobilization of I onto WO_3 framework may be responsible for the distortion of lattice fringes and induction of more defects on WO_3.

On the contrary, a clearer lattice fringes without distortion was observed as the concentration of P was increased, which implies that most of the P were entrapped within the space of WO_3 framework. Furthermore, the d-spacing in the HRTEM micrograph also aligned well with the d–spacing calculated from the XRD patterns. The SAED pattern confirmed that the prepared material is well crystallized nanoparticles grown along the [002] direction (Tokunaga et al., 2012). The HRTEM images show that the average interplanar distance of both mono and co-doped WO_3 nanomaterials was about 0.336 nm corresponding to crystal

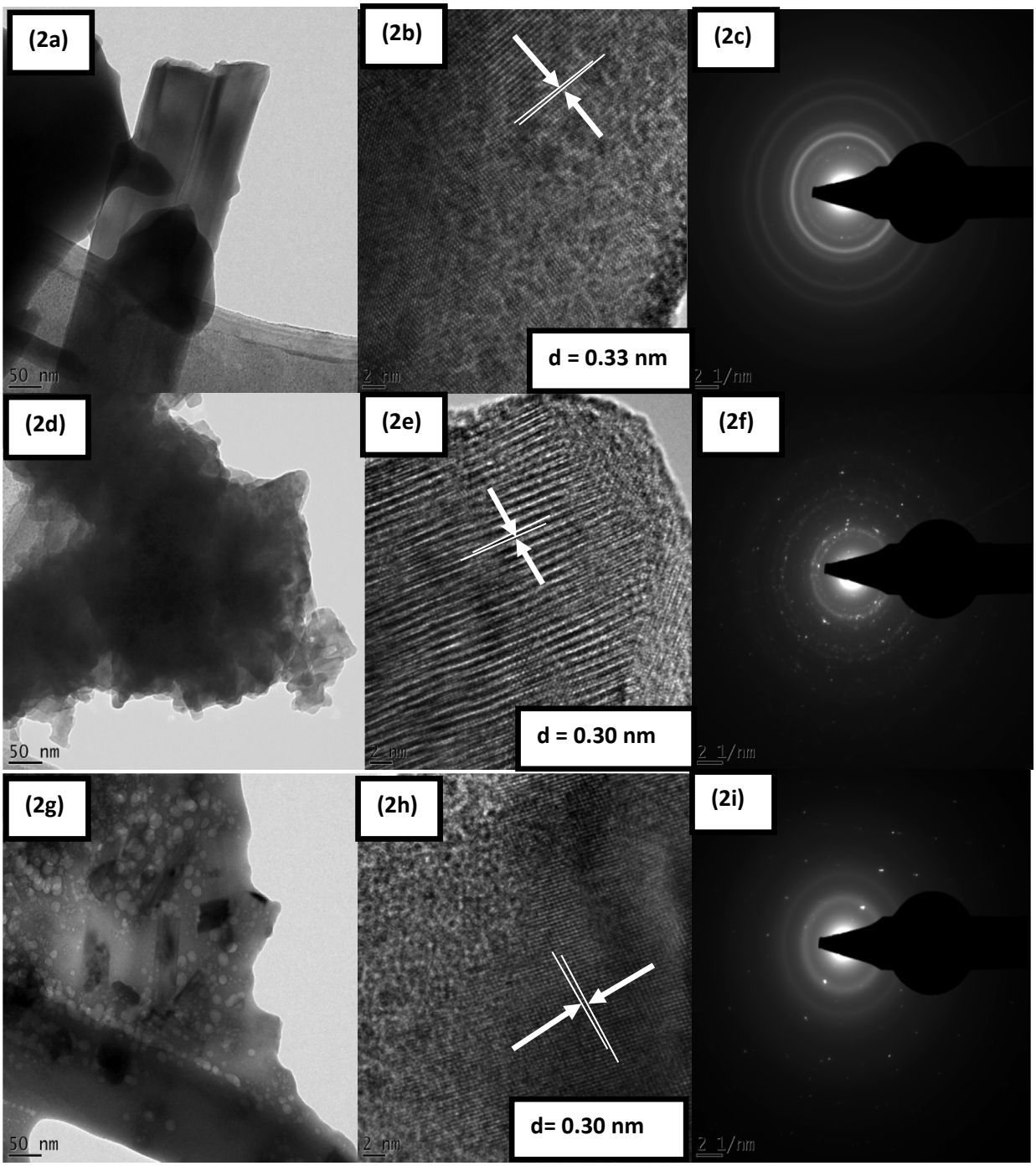

Fig. 5. (2a) & (2b) HRTEM images for 2% P-WO_3 nanocomposites, (2c) SAED images for 2% P-WO_3. (2d) & (2e) HRTEM images for 5% P-WO_3, (2f) SAED images for 5% P-WO_3. (2g) and (2h) HRTEM images for 10% P-WO_3, (2i) SAED images for 10% P-WO_3.

plane [002] (Morales et al., 2007). The incorporation of I^- and P^{+3} in the WO_3 framework plausibly caused distortion of the lattice fringes of WO_3 and induced more defects (see Fig. 6 (7a, 7b)) (Song et al., 2010). Similar results were reported for the growth of WO_3 nanoparticles along the [002] crystal plane by Harshulkhan et al. (2016) for Ag doped WO_3. Conversely, Mu et al. (2015) reported that Nb-doped WO_3 preferred to grow along [001] planes. The difference in the crystal planes and pattern of growth can be ascribed to the nature of the dopant used and method of synthesis.

3.3. Elemental composition of I-doped WO_3, P-doped WO_3 and I-P-doped WO_3 nanocomposites

Fig. 7 revealed the presence of tungsten, and oxygen in different proportions. Although, the dopants (iodine and phosphorus) were not detected by the EDS probably due to their low concentration in the matrix. However, carbon present in the sample may be from the holey carbon grids or plant extract used during the synthesis.

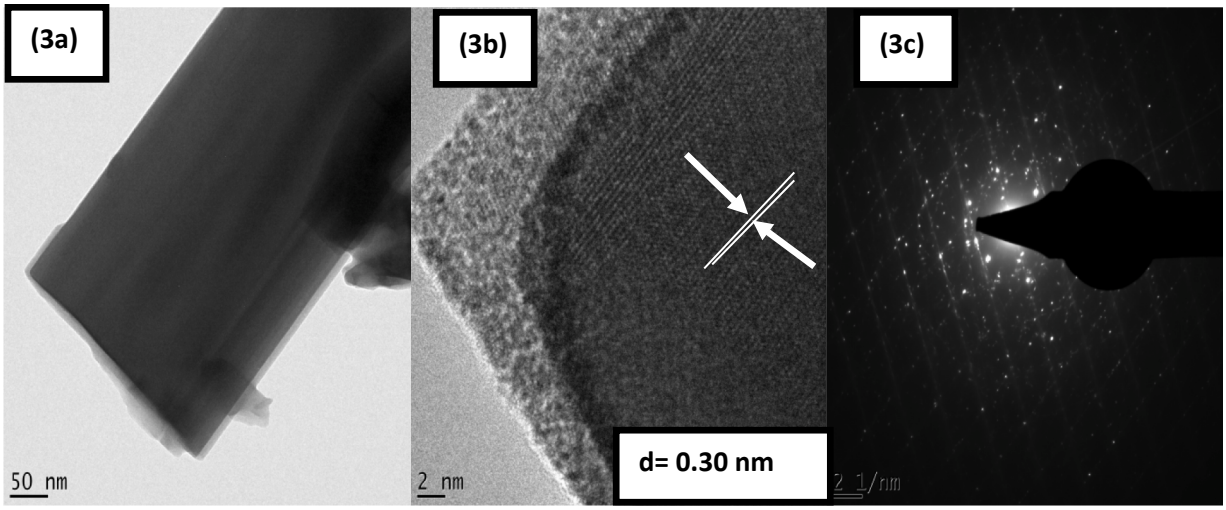

Fig. 6. (3a) and (3b) HRTEM images for 2% I-P-WO_3, (3c) SAED images for 2% I-P-WO_3.

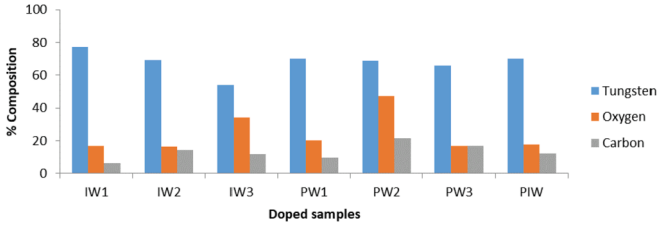

Fig. 7. Elemental composition of WO_3 doped samples at various % of I and P dopants. XRD pattern for I-doped WO_3, P-doped WO_3 and I-P-WO_3 nanocomposites.

3.4. XRD pattern for I-doped WO_3, P-doped WO_3 and I-P-WO_3 nanocomposites

The XRD patterns of pure and mono-doped I-WO_3, P-WO_3 and co-doped I-P-WO_3 nanocomposites are shown in Fig. 8.

The XRD spectra of the pure WO_3 demonstrated the presence of three intense diffraction peaks at 2θ values of 23.18°, 23.66°, and 24.38°

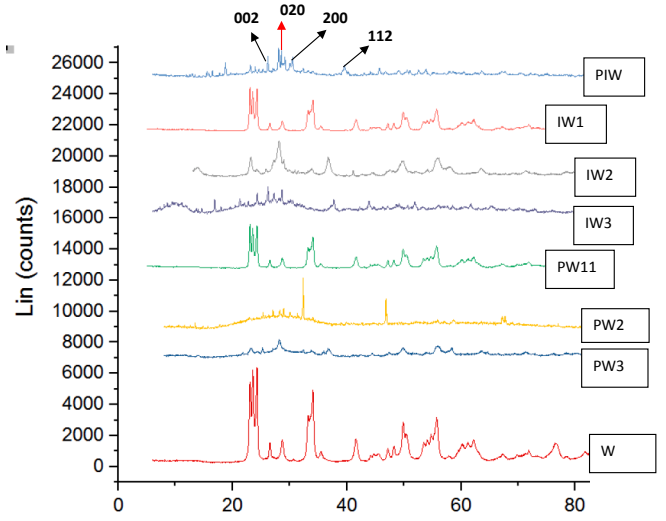

Fig. 8. XRD patterns (W) WO_3 nanoparticles alone (IW1) 2% Iodine doped WO_3 (IW2) 5% Iodine doped WO_3, (IW_3) 10% Iodine doped WO_3 (PW1) 2% Phosphorus doped WO_3 (PW2) 5% Phosphorus doped WO_3, (PW_3) 10% Phosphorus doped WO_3 (PIW) 2% co-doped phosphorus and iodine nanocomposite.

with their corresponding crystal planes of (002), (020), and (200). The WO_3 produced is assigned body-centered tetragonal which is in agreement with the Joint Committee on Powder Diffraction Standards (JCPDS) No.00-041-0905 for monoclinic phase. The intensity of the (002) facets was much stronger than that of the other facets observed in the XRD spectrum and the average crystalline size calculated from the Scherer equation was in the range of 5.9–8.3 nm. Similarly, for the mono doped I and P doped WO_3 samples, the diffraction peaks could be indexed to monoclinic structure of WO_3. The average crystalline sizes for 2%, 5% and 10% I doped WO_3 were found to be in the range of 1.0–1.2 nm, 1.24–1.89 nm and 1.31–2.32 nm respectively. While, the crystalline sizes of 2%, 5% and 10% P doped WO_3 nanoparticles were 2.28–3.46 nm, 6.37–7.11 nm, 8.28–10.80 nm respectively. It was noticed that the crystalline size increase with concentration of the dopants. Li et al. (2012) observed increase in crystalline size upon when the concentration of sulphates was increased on the lattice layer of WO_3 nanoparticles.

For the I and P-doped WO_3 samples no peak corresponding to iodine or phosphorous were detected due to their low concentration. This suggests that the grain sizes of phosphorus successfully diffused while iodine were well dispersed onto the crystal lattice of WO_3 nanoparticles. In addition, the calculated lattice parameters value (a = 7.3702, b = 12.5891 and c = 7.7789) decreases after doping with iodine and phosphorus. This is probably due to the smaller ionic radius of P^{3+} (0.038 nm) when compared to that of tungsten W^{6+} (0.062 nm), that of iodine was larger (0.2 nm) leading to the distortion of the crystallographic nature of the nanomaterial. The smaller ion P^{3+} can easily enter the W crystal site. Some of the W^{6+} ions were replaced by the P^{3+} ions and doped with substitutional and regular lattice site thus responsible for the decreased grain size and enhanced the surface area of pure WO_3. While for the case of iodine doped WO_3, I^- ion substitutionally replaced O^{2-} in WO_3. This substitution is expected to be quite destructive to the lattice as I^- is much larger than O^{2-} (0.2 nm vs 0.14 nm). Similar result was reported by Rettie et al. (2014), where WO_3 prepared by spray pyrolysis was separately doped with sulphur and iodine and the authors concluded that both the ionic radius of sulphur and iodide are larger than oxygen and should expand the lattice. However, in this study the amount of these dopants were too low to induce crystallographic changes as detectable by XRD. It was also noted that the intensity of most predominance peaks (triplet) with miller indices (002), (020) and (200) decreased and full width at half maximum (FWHM) increases with increasing iodine and phosphorus dopant concentration from 2 to 10%. The crystalline size of I-P co-doped WO_3 nanocomposites was in the range of 3.76–3.84 nm.

Table 1
Surface area and pore data parameters for WO_3 and I-WO_3, P -WO_3 and I-P-WO_3.

S/N	Photocatalyst	Surface area (m^2/g)	Pore size (nm)
Commercial	WO_3	19.42	0.03
	WO_3	352.49	2.13
	P-WO_3	356.76	2.14
	I-WO_3	392.50	2.14
	I-P-WO_3	416.33	2.10

3.5. BET results for the synthesized WO_3 nanocomposites

Table 1 shows the surface area and pore size distribution for the synthesized nanomaterials.

From Table 1, it is obvious that the surface area of the as-synthesized nanoparticles and composites changed, even though no significant differences were noticed in the Barret-Joyner-Halenda (BJH) pore size. A significant increase in surface area was noted for doped I-P-WO_3 compared to the undoped WO_3. However, it appeared that the surface area of the mono-doped with either I_2 or P did not significantly improved. A synergistic mechanism of the two elements showed promising improvement in the surface area when added in appropriate proportions. The increment in the surface area could be attributed to increase intercalation of P^{+3} and substitution of I^- for interstitial oxygen between the structure of WO_3 network. Similar result was reported by Song et al. (2014), where the surface area of WO_3 nanoparticles synthesized using the template method increased from 201 to 225 m^2/g upon loading with 5% Fe. However, the surface area obtained in this study almost doubled that reported by Song et al. (2014). This is attributed to the dopant type and co-doping phenomenon. It should be mentioned that the surface area of WO_3 nanoparticles is 15 times higher than the available commercial WO_3 and this can be attributed to the nature of tungsten precursor and method of synthesis.

3.6. UV–visible absorption and energy gap calculation

The UV–Visible absorption spectra of WO_3, P-WO_3, I-WO_3 and I-P co-doped WO_3 nanocomposites is shown in Fig. 9. The mono and co-doping of WO_3 nanoparticles with either I or P or both resulted to considerable red shifting in absorption threshold value to longer wavelength (350–495 nm) and visible light region.

The absorption data of each sample were used to obtain the optical band gap using Tauc's equation, which shows a relationship between incident photon energy of semiconductors and the absorption coefficient as shown in Equation (3).

$$khv^{\frac{1}{n}} = B(hv - E_g) \quad (3)$$

where B is a constant, the exponent n is taken as for indirect band gap as 2, and Eg is an optical band gap of the material. The energy band gap

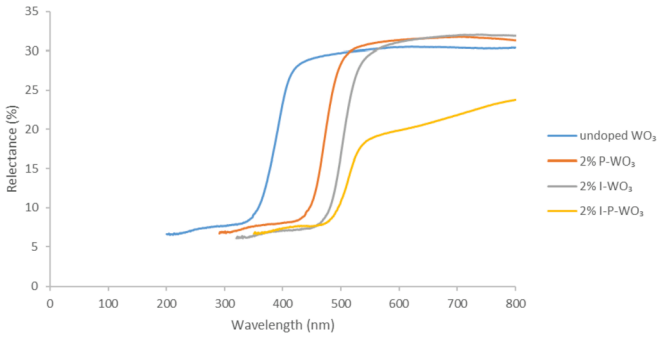

Fig. 9. UV–Visible spectra for undoped WO_3, P-doped WO_3, I-doped WO_3 and I-P, co-doped WO_3 nanomaterials.

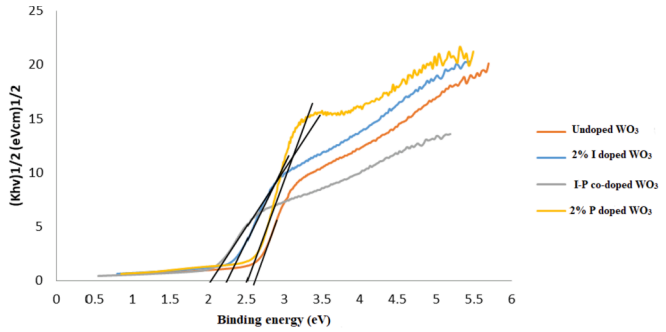

Fig. 10. Tauc's plot from which the bandgap of the prepared WO_3 and I-P co-doped WO_3 nanocomposites.

(Eg) of the synthesized samples shown in Fig. 10 was obtained by plotting $(khv)^{1/2}$ versus hν and extrapolating the linear portion of the absorption edge. The k in the Tauc formula can be replaced with the Kubelka-Munk function F (R) calculated as $F(R_\infty) = (1- R_\infty)^2/2R_\infty)$ where $R(_\infty)$ is diffuse reflectance of the sample relative to the reflectance of a standard according to the Kubelka-Munk theory. The % diffuse reflectance was then plotted vs the wavelength.

As shown in Fig. 10, the band gap energy for undoped WO_3 was 2.61 eV which fall within the band gap values reported from literature (2.6 eV–3.2 eV) (Washizu et al., 2003). However, after doping and co-doping with I and P, the band gap of WO_3 reduced to 2.41 eV, 2.17 eV and 2.02 eV for P-WO_3, I-WO_3, and I-P-WO_3 respectively. The reduction in band gap energy of WO_3 may be attributed to the alteration, dislocation and distortion of the microstructural and morphological framework of the prepared WO_3 by I and P. This further suggest significant suppression of the photo-electron-hole recombination rate. Comparing the band gap energy of I-WO_3 and P-WO_3, it was noticed that WO_3 nanoparticles doped with 2% Iodine showed narrower band gap than 2% Phosphorus doped. This can be attributed to interstitial effect of Iodine than Phosphorus that exhibited more of substitutional behaviour (Chang et al., 2011).

The reduction in the band gap energy can be explained as follows. Firstly, the doping of I and P ions may be responsible for the introduction of acceptor energy levels below the conduction level of WO_3. Secondly, both I and P ions adsorbed on the surface of WO_3 favoured the separation of the charge carriers, prolonging the life of carriers, and suppressed the recombination of photo-generated electron–hole pairs (Gonzalez-Ortega et al., 2006). The I-P co-doped WO_3 had the smallest band gap energy due to alteration of the crystal and electronic structures of WO_3 by both I and P. Similarly, Mu et al. (2015) reported that doping WO_3 nanoparticles with niobium was responsible for the reduction of band gap energy from 2.83 to 2.60 eV. Similarly, Rettie et al. (2014) successfully doped iodine and sulphur on WO_3 films and decrease in bandgap (from ~2.7 to 2.6 and 2.1 eV respectively) at 2% dopant concentration each were observed.

3.7. XPS analysis for the synthesized doped and undoped WO_3 nanocomposites

The result of the general XPS survey of WO_3, I-WO_3 P-WO_3 and I-P-WO_3 is shown in Fig. 11. As shown in Fig. 11, it can be seen that the doped nanocomposite contained W, O, C, I and P elements and theirs corresponding photoelectron peaks orbital were, W (4f), O (1s), C (1s), I (3d) and P (2p), respectively. Fig. 11a showed the deconvoluted XPS scan of W (4f) core and demonstrated the presence of two peaks in the binding energies of 35.6 eV and 37.6 eV which corresponds to $W4f_{7/2}$ and $W4f_{5/2}$ reported in the literatures for a typical WO_3 nanoparticles (Liu et al., 2012) (Fig. 11b). These two separate broad peaks with no shoulder in between correspond to W element with oxidation state of +6. In the same vein, another low intensity doublet peaks observed in

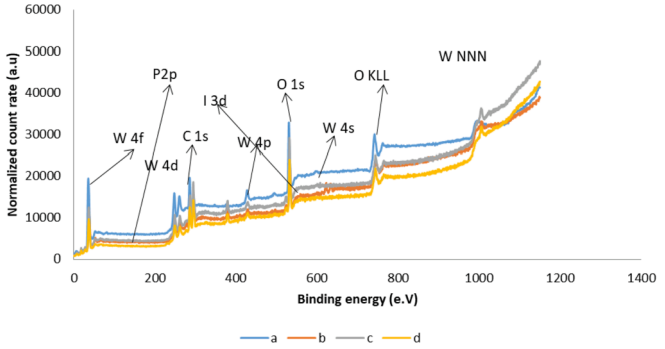

Fig. 11. a. XPS survey of (a) undoped WO_3, (b) 2%I-WO_3, (c) 2%P-WO_3 and (d) 2%I-P-WO_3, 11b XPS survey W (4f) region. 11c. XPS survey I (3d) signals. 11d. XPS survey P (2p) signals.

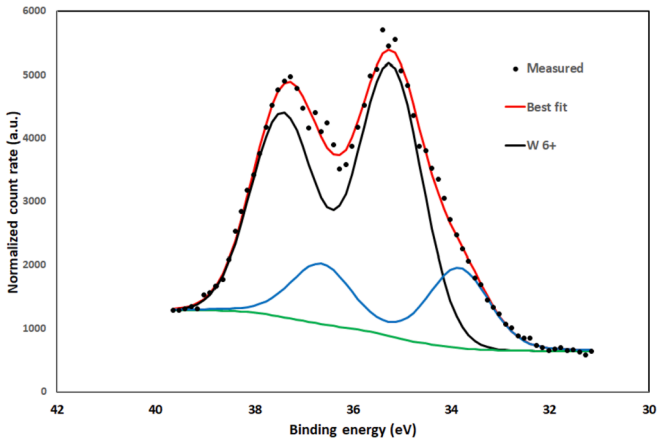

Fig. 11. (*continued*)

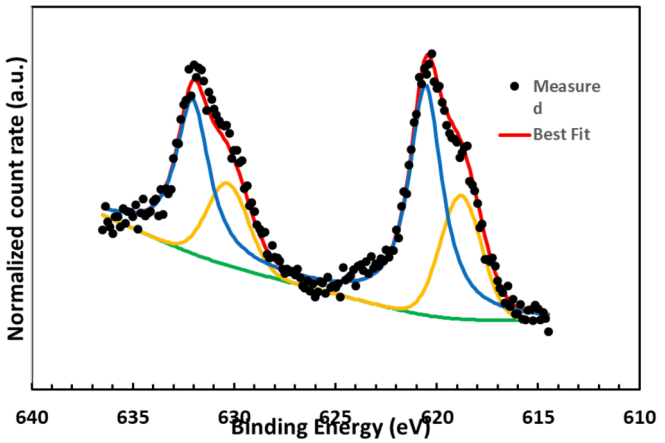

Fig. 11. (*continued*)

binding energies of 34.6 and 37.2 eV suggested the existence of W in +5 oxidation state. Thus, the W element in the nanoparticle existed in the form of W^{6+} and W^{5+} and further indicate the presence of oxygen vacancies (O^{2-}). It is obvious that there were two contributions to W (4f) energy envelope within WO_3 framework namely; stoichiometric (WO_3) and non-stoichiometric contribution (WO_{3-x}). The non-stoichiometric (WO_{3-x}) suggests the existence of O^{2-} vacancies and that the two dopants possibly replaced the lattice oxygen in stoichiometric WO_3. The phenomenon of oxygen vacancies may be responsible for the reduction of the band gap energies of the synthesized nanomaterials (see Fig. 10). Additionally, W (4f) and O (1s) with binding energies of 35.7 eV and 530.5 eV respectively agreed well with reported XPS spectra of WO_3 (Blackman and Parkin, 2005). In the case of I-doped WO_3, iodine peak

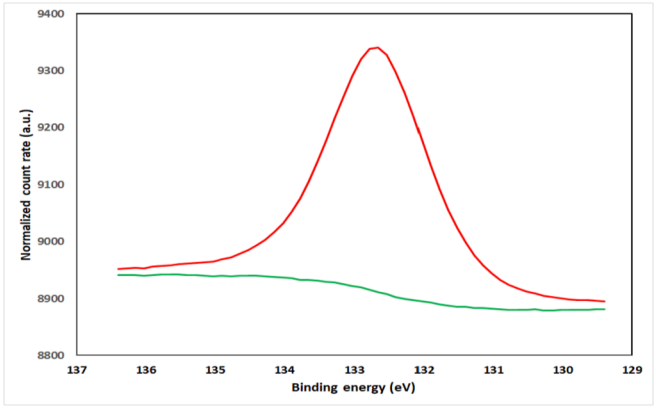

Fig. 11. (*continued*)

found at binding energy of 619.5 eV (Fig. 11c), belongs to $3d_{5/2}$ orbital (Tojo et al., 2008). While the enveloped P was detected at the binding energy of 134.5eV as shown in (Fig. 11d). The XPS analysis confirmed successful incorporation of both impurities (I_2 and P) onto WO_3 framework.

Table 2 shows the result of the physico-chemical assessment of the local dyeing wastewater and it was noticed that the indicator parameters (TOC and COD) decreased after photocatalytic interaction. As shown in Table 1, it can be noticed that the level of COD and TOC in the raw wastewater is significantly higher due to the excessive usage of organic dyes and chemicals during dyeing activities. It is worthy to note that the BOD/COD ratio of approximately 0.37 further confirmed the presence of considerable numbers of non-biodegradable organic dyes. Thus direct discharge of such wastewater containing toxic organic dyes into water bodies without proper treatment will constitute serious environmental challenge not only to human but also aquatic species.

3.8. Photocatalytic activity

The photocatalytic activity of the as-synthesized WO_3 samples were investigated based on their capability to mineralize local dyeing wastewater under natural sunlight irradiation (> 420 nm). The percentage degradation efficiency of the local dyeing wastewater measured in terms of TOC and COD by the catalyst under sunlight as a function of irradiation time is shown in Figs. 12 and 13 respectively. The blank experiment with sunlight alone in the absence of catalyst as well as catalyst without light was also performed. It is evident that there was no degradation of the organic dyes in the dyeing wastewater in the presence of sunlight or catalyst alone under the same irradiation time, which suggest that the degradation of dye molecules did not follow either photolysis or adsorption technology.

In Figs. 12 and 13, it was generally observed that the photocatalytic performance of I-P co-doped WO_3, I-doped WO_3, P-doped WO_3 and undoped WO_3 samples increased with irradiation time. At every irradiation time, I-P co-doped WO_3 nanocomposite has much higher photocatalytic activity than mono and undoped WO_3 nanoparticles. In comparison to undoped WO_3, it is interesting to note that I-doped WO_3 showed a relatively higher activity than P-doped WO_3 nanoparticles. This was possible because I^- act as an electron donor, and created W^{6+} vacancies and balanced excessive charges, thus responsible for its lower band gap energy, high surface area and enhanced photooxidation ability.

As can be seen in Table 1, Iodine doping level was more pronounced on the BET surface areas of WO_3 than Phosphorus and thus the observed improvement of the photoactivity for the I-doped WO_3 than P-doped WO_3 can be linked to the Iodine doping, which was responsible for the increases in the degradation of organic dyes amount, and light absorbance of catalyst. Furthermore, the Iodine doping may be also good for the reduction of recombination rate of photo-generated electron hole carriers and the

Table 2
Physiochemical parameters of Local dyeing wastewater from Kofar mata dye pits Kano.

Parameters	Result before photocatalytic degradation	Result after photocatalytic degradation with I-P co-doped WO_3	International standard (WHO and FEPA)
Colour	Dark-red	Mild red- clear	colourless
Odour	Fishy	odourless	odourless
Appearance	Cloudy	Clear	clear
Temperature (°C)	27.0 ± 0.01	25 ± 0.02	23.5–30
pH	6.2 ± 0.01	8.1 ± 0.03	6.0–9.0
TDS (mg/dm^3)	843.0 ± 0.07	375 ± 0.01	500
Conductivity (ms/cm)	700.6 ± 0.01	1200 ± 0.01	1000–2000
Chemical oxygen demand (mg/dm^3)	991 ± 0.01	44.2 ± 0.02	< 120.00
Biochemical oxygen demand (mg/cm^3)	368.15 ± 1.13	29.56 ± 0.04	< 50.00
Turbidity (NTU)	69.47 ± 0.01	2.5 ± 0.01	5.00
Total organic content (mg/dm^3)	576.8 ± 0.01	16 ± 0.02	< 75.00

FEPA = Federal Environmental Protection Agency (Wastewater discharge (1991)).
WHO = World Health Organization (2011).

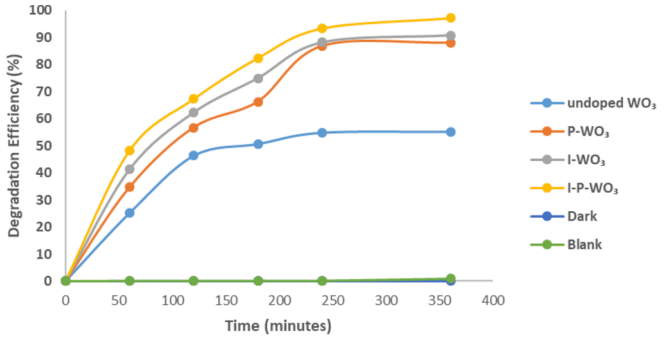

Fig. 12. Degradation efficiency of TOC in local dyeing wastewater by WO_3 nanomaterials. (Experimental conditions: volume of wastewater (100 cm^3), stirring speed (150 rpm), catalyst dosage (1 g), pH of the wastewater (5)).

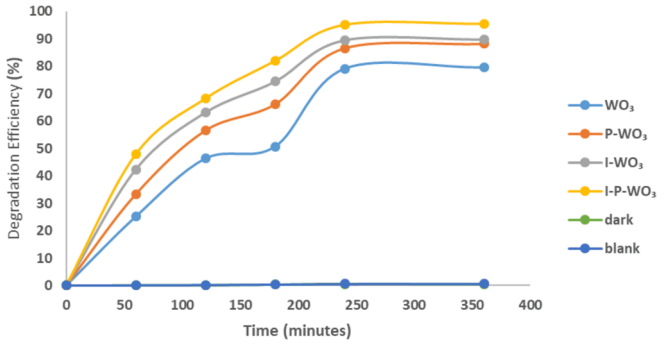

Fig. 13. Degradation efficiency of COD in local dyeing wastewater by WO_3 nanomaterials. (Experimental conditions: volume of wastewater (100 cm^3), stirring speed (150 rpm), catalyst dosage (1 g), pH of the wastewater (5)).

increase in interfacial charge-transfer efficiency, consequently, the overall photoactivity of the catalyst. Comparing with undoped WO_3, P-doped WO_3 photocatalyst successfully degrade organic dyes in the wastewater than WO_3 alone as shown in Figs. 12 and 13 due to the lower band gap energy (2.41 eV) and higher surface area (356.76 m^2/g) of the former than the latter with band gap energy and surface area of 2.61 eV and 352.49 m^2/g respectively. The maximum degradation of the dye molecules at irradiation time of 240 min by the photocatalysts; I-P/WO_3, I/WO_3, P/WO_3 and bare WO_3 samples were in the order 93.40 > 88.19 > 86.80 > 54.86% for TOC and 95.14 > 89.14 > 86.63 > 79.17% for COD respectively (see Figs. 12 and 13). Beyond 240 min, it was noticed that further increase in the irradiation time during the photocatalytic activity of synthesized catalysts remained unchanged. It can be observed that I-P co-doped WO_3 clearly demonstrated enhanced degradation efficiency for both parameters at 93.40% and 95.14% for COD and TOC than other photocatalysts and the order of the performance were I-P-WO_3 > I-WO_3 > P-WO_3 > WO_3. The increased photocatalytic efficiency of the I-P co-doped WO_3 may be ascribed to decrease crystalline size of WO_3 and the higher surface area due to existence of synergy between the two dopants. Along with the decreased grain size and enhanced the surface area of pure WO_3, the incorporation or diffusion of Iodine and Phosphorus onto the surface matric of WO_3 maybe created a surface defects or distortion of the crystallographic nature of the nanomaterial and by extension responsible for the enhanced photoactivity efficiency. It can be seen that the photocatalytic behaviour of nanomaterials were closely related to their band gap energy, surface area, microstructures, and dopant types. It is interesting to note that the I-P co-doped WO_3 nanoparticles exhibited improved photocatalytic activities compared with the undoped WO_3 nanoparticles due to the decreased the band gap of WO_3 shown in Fig. 10 attributable to the acceptor energy levels below the conduction level of WO_3.

Additionally, the active surface area of nanoparticles is important to the photocatalytic property. According to a Brunauer–Emmett–Teller (BET) analysis shown in Table 1, it is obvious that the surface areas of undoped WO_3 improved significantly upon mono and co-doping with I and P, which resulted in increasing active sites and further enhanced its photocatalytic activity. For instance, the photocatalytic activity of I-P-WO_3 with active surface area of 416 m^2/g is 1.16 times greater than the undoped WO_3 with surface area of 352.49 m^2/g. Therefore, the I-P co-doped WO_3 nanocomposites have higher solar energy conversion efficiencies than that of the undoped WO_3, thus responsible for the improved photocatalytic activity. In Fig. 10, it was noticed that the optical band gap energy of I-P-WO_3 (2.02 eV) is smaller than 2.61 eV for the undoped WO_3. This implies that the I-P-WO_3 photocatalyst with the lowest band gap could convert solar energy better than undoped or mono doped WO_3 and hence enhanced photocatalytic activity. The amount of I and P adsorbed on the surface of WO_3 favoured charge carrier separation and prolong the life of carriers, prevent the recombination of photo-generated electron–hole pairs and eventually enhanced the photocatalytic activity The improved photocatalytic activity of I-P co-doped WO_3 could be linked to controlled morphologies and microstructures, fast and efficient separation of charge carriers as well as suppression of the rate of the recombination of photo-generated electron–hole pairs by I and P. This significance red shift is an evident of excellent photocatalytic degradation of local dyeing wastewater by each prepared photocatalyst as nanomaterial with a smaller bad gap of 2.04 eV in this case I-P-WO_3 exhibited improved activity under sunlight compared to undoped WO_3 with a higher bandgap of 2.61 eV. In summary, the synthesis methods, surface area, band gap energy, dopant types considerably influence the photo-oxidation behaviour of the catalyst towards the pollutants and, consequently determined the overall photoactivity of the photocatalytic process.

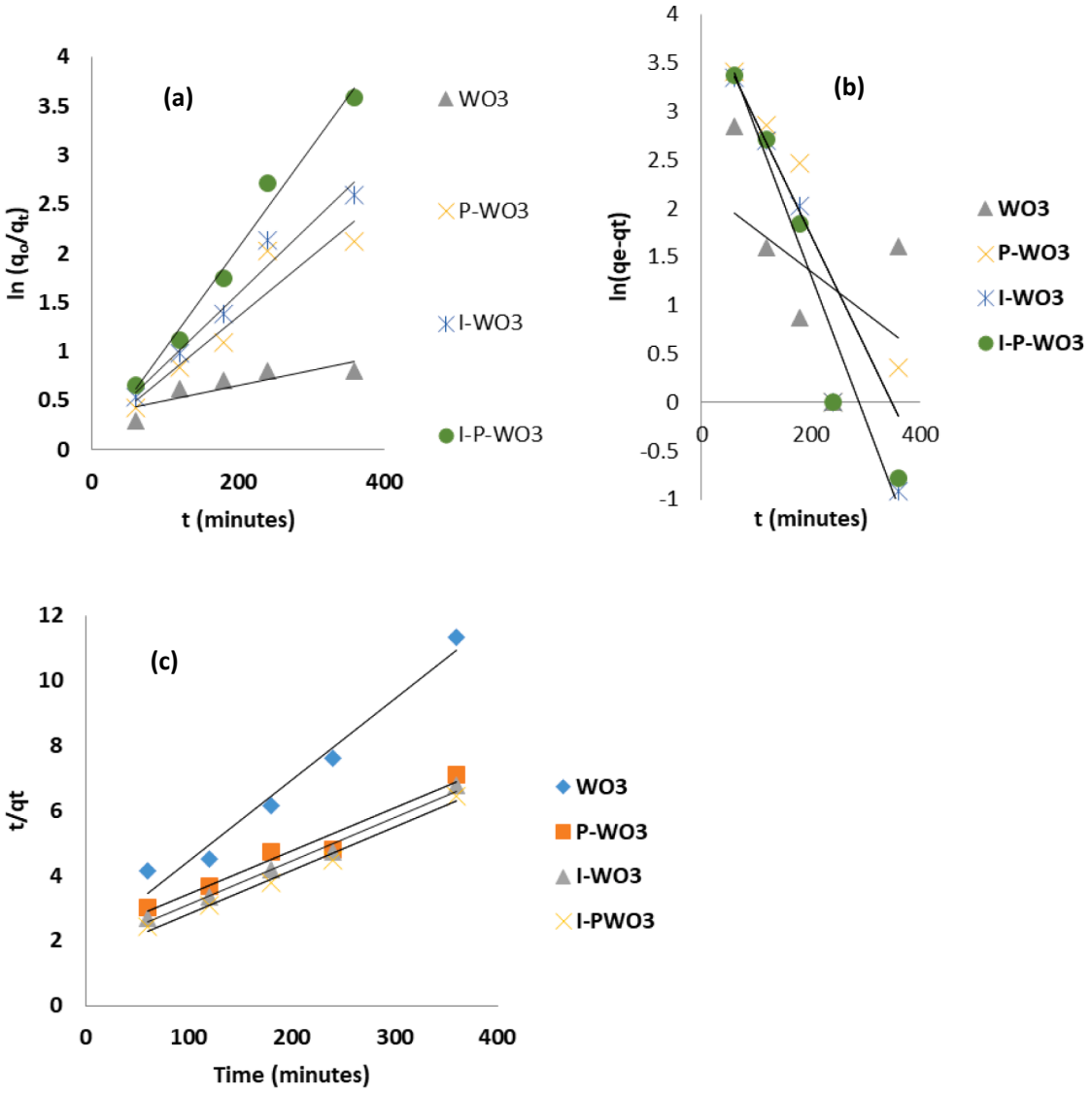

Fig. 14. (a) First order (b) Pseudo-first order (c) Pseudo-second order plot of the degradation of TOC in local dyeing wastewater by WO_3 nanomaterials.

Kinetics studies for the Photo-degradation of local dyeing wastewater by WO_3 nanomaterials.

To further understand the degradation rate of local dyeing wastewater in the presence of WO_3 nanomaterials; three different kinetic models namely; first order, pseudo first order and pseudo second order kinetic models were used to fit in the experimental data. For the first order kinetics, the first-order rate constant (k) were calculated using equation (4).

$$\ln\left(\frac{q_0}{q_t}\right) = -K_1 t \tag{4}$$

where q_0 and qt are the concentration of dyeing wastewater (mol/dm^3) in aqueous solution at times zero (0) and t, t is the time of irradiation and k is the rate constant in (min^{-1}) (He et al., 2013).

A graph of $ln\frac{q_0}{q_t}$ against t was plotted (Figs. 14 (a) and 15 (a)) and the calculated results are shown in Table 3.

According to Table 3, it can be noticed that the value of rate constant k (0.01 min^{-1}) for the co-doped composite I-P-WO_3 is 10 times higher than pure WO_3 (0.001 min^{-1}). Similar trend was observed for the other two models. However, Song et al. (2014) found that the degradation of Rhodamine blue by Fe-doped WO_3 was 28 times faster than pure WO_3 alone using first order kinetic. The rate constant obtained is this study is small compared to that obtained by Song et al. (2014). This may be attributed to the nature of the wastewater used. In this study, there was strong competition for the target pollutant by both the radical scavengers (CO_3^{2-}, SO_4^{2-}, NO_3^-) with hydroxyl radicals (OH·) generated by WO_3 in the solution. These radicals' scavengers inhibited the performance of the hydroxyl radicals and thus responsible for the low rate constant. In the case of Song et al. (2014) simulated solution containing no radicals was used. Hence there was no strong competition for the target pollutants such as available OH radicals which were free to degrade Rhodamine blue.

For pseudo first order kinetics, the equation (5) is expressed as

$$\ln(q_e - q_t) = lnq_e - k_1 t \tag{5}$$

where q_e and q_t depict the amount of adsorbed pollutant (mg/g) at equilibrium and at any instant of time t (min), respectively.

A plot of $\ln(q_e - q_t)$ against t give a straight line (Figs. 14 (b) and 15 (b)) with q_e as the intercept and k_1 as the slope, which represent the rate constant of pseudo first order adsorption operation (min^{-1}). And for the second order kinetics; the equation can be expressed as;

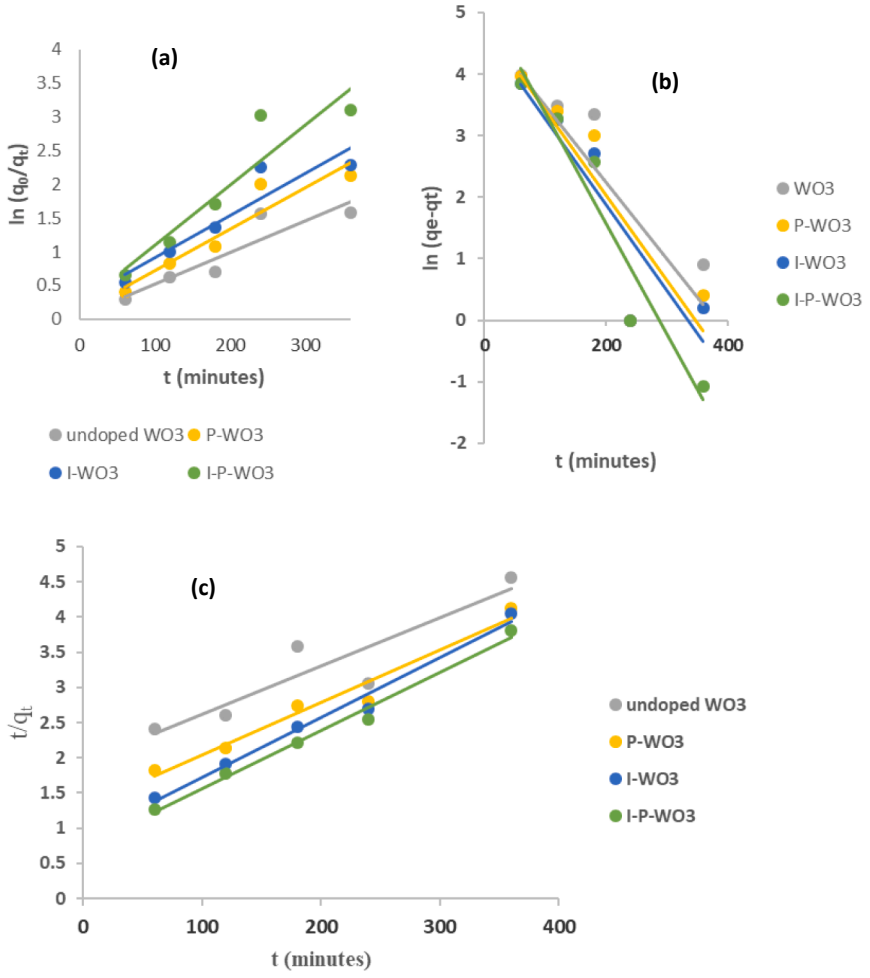

Fig. 15. (a) First order (b) Pseudo-first order (c) Pseudo-second order plot of the degradation of COD in local dyeing wastewater by WO_3 nanomaterials.

$$\frac{t}{q_t} = \frac{1}{q^2K_2} + \frac{1}{q_c}t \quad (6)$$

where k_2 is the equilibrium rate constant of pseudo second-order adsorption ($gmg^{-1}min^{-1}$).

A plot of $\frac{t}{q_t}$ versus t (Figs. 14 (c) and 15 (c)) should give a linear relationship which allows the computation of a second-order rate constant, K_2 and q_e. The values of the k_1 and k_2 by the different WO_3 nanomaterials are also shown in Table 4.

As shown in the Tables 3 and 4, the rate constant (k_1 or k_2) and correlation coefficient (R^2) for the pseudo-second order models is higher than first order and pseudo first order. The order of fitness in terms of R^2-values by the photocatalyst are I-P-WO_3 > I-WO_3 > P-WO_3 > WO_3 for both TOC and COD. Again, the differences in the rate constant and R^2 may be attributed to the different surface area, particles and band gap energy of the prepared nanomaterials. The fitness of the data to pseudo-second order model suggests that the degradation of the dye molecules in the wastewater depends on the concentration of the dye molecules in the wastewater and the dosage of the catalyst. Similar results have been reported by Shirvastava (2012), for the degradation of methylene blue by TiO_2 nanocrystals and the kinetics was consistent with pseudo second order compared to pseudo first order kinetics.

4. Conclusion

In summary, WO_3 nanoparticles were successfully synthesized from

Table 3
Kinetic parameters for the degradation of TOC in local dyeing wastewater by WO_3 nanomaterials.

Photocatalyst	First-order			Pseudo First-order			Pseudo Second-order	
	$\ln(\frac{q_0}{q_t}) = -k_1t$			$\ln(q_e - q_t) = \ln q_e - k_1t$			$\frac{t}{q_t} = \frac{1}{q_e^2k_2} + \frac{1}{q_e}t$	
	k_1	R^2	q_e	k_1	R^2	q_e	k_2	R^2
WO_3	0.001	0.700	1.25	0.004	0.224	41.67	8.0×10^{-3}	0.964
P- WO_3	0.006	0.886	58.09	0.011	0.773	76.02	1.2×10^{-2}	0.969
I- WO_3	0.007	0.966	58.09	0.012	0.871	76.92	1.4×10^{-2}	0.992
I-P-WO_3	0.01	0.981	67.55	0.014	0.945	77.85	2.9×10^{-2}	0.994

Table 4
Kinetic parameters for the degradation of COD in local dyeing wastewater by WO_3 nanomaterials.

Photocatalyst	First-order			Pseudo First-order			Pseudo Second-order	
	$\ln(\frac{q_0}{q_t}) = -k_1 t$			$\ln(q_e - q_t) = \ln q_e - k_1 t$			$\frac{t}{q_t} = \frac{1}{q_e^2 k_2} + \frac{1}{q_e} t$	
	k_1	R^2	q_e	k_1	R^2	q_e	k_2	R^2
WO_3	0.0047	0.846	113.51	0.004	0.660	144.92	1.8×10^{-1}	0.836
P- WO_3	0.0062	0.894	122.39	0.011	0.767	133.33	2.9×10^{-1}	0.961
I- WO_3	0.0062	0.871	107.65	0.012	0.811	117.65	4.9×10^{-1}	0.985
I-P-WO_3	0.089	0.877	122.39	0.014	0.945	120.48	5.6×10^{-1}	0.989

mixture of ammonium paratungstate and *Spondias mombin* plant extract by simple green method. The co-doping of the prepared WO_3 nanoparticles with I and P and photocatalytic performance were evaluated for the degradation of local dyeing wastewater. Predominantly monoclinic WO_3 nanoparticles with particle size of 13.8 nm was obtained at pH at 1 and calcination temperature 550 °C under air. In addition, HRTEM/HRSEM results revealed complete transformation of the spherical synthesized WO_3 nanoparticles to rod-like and bamboo bundles depending on the nature of the dopant. The WO_3 nanoparticles grown predominantly in the [002] plane irrespective of the dopants and BET surface area of the samples was in the order of I-P-WO_3 > I-WO_3 > P-WO_3 > WO_3 such as 416.33 > 392.50 > 356.76 > 352.49 m^2/g respectively. The XPS analysis revealed the substitutional and interstitial occupation of oxygen vacancies in WO_3 framework by I^- and P^{+3} ions. The band gap energy reduction was dependent on the dopant type however smaller value was obtained under co-doping phenomenon indicating a red shifted in the presence of iodine and phosphorus. The I-P co-doped WO_3 nanocomposites exhibited the highest photocatalytic activity of about 93.40% and 95.14% for TOC and COD reduction respectively, when compared to mono-doped and un-doped WO_3 samples. It was found that materials with low band gap energy, higher BET surface area and more porous structure demonstrated much higher photocatalytic activity. The kinetics of the reaction revealed that the reaction with co-doped WO_3 nanocomposites was 10 times faster compared to the undoped WO_3 nanoparticles, while the kinetics best fitted to pseudo second order model. This study provides new insights for the preparation of highly photoactive I-P co-doped WO_3 nanomaterials with higher specific surface area, smaller band gap energy, good crystallinity and monoclinic crystal polymorph for the degradation of local dyeing wastewater.

Acknowledgements

The authors acknowledged the financial support received from Tertiary Education Trust Fund (TETFUND), Nigeria under a grant number TETFUND/FUTMINNA/2018/001. The technical assistance received from the following people: Dr Remy Bucher (XRD, ithemba Labs, South Africa), Dr. Franscious Cummings (Electron Microscope Unit, Physics department, University of the Western Cape, South Africa) and Prof. W.D. Roos (Physics department, University of the Free State, South Africa) in term of HRTEM/HRSEM and XPS analysis is highly appreciated.

References

Aminian, M.K., 2009. Morphology influence on photocatalytic activity of tungsten oxide loaded by platinum nanoparticles. J. Mater. Res. 25 (1), 141–148.
Asim, N., Badeiei, M., Ghoreishi, K.B., Ludin, N.A., Zonooz, M.R.F., Sopian, K., 2013. New Developments in photocatalysts modification: case study of WO_3. Adv. Fluid Mech. Heat Mass Tran. 1109–1116 ISBN: 978-1-61804-114-2.
American Public Health Association (APHA), 2012. Standard Methods for the Examination of Water and Waste Water, twenty-second ed. APHA, Washington D.C.
Baruah, S., Pal, S.K., Dutta, J., 2012. Nanostructured zinc oxide for water treatment. Nanosci. Nanotechnol. - Asia 2 (2), 90–102.
Barakat, N.A.M., Kanjwal, M.A., Chronakis, I.S., Kim, H.Y., 2013. Influence of temperature on the photodegradation process using Ag-doped TiO2 nanostructures: negative impact with the nanofibers. J. Mol. Catal. Chem. 366, 333–340.
Blackman, C.S., Parkin, I.P., 2005. Atmospheric pressure chemical vapor deposition of crystalline monoclinic WO_3 and WO_{3-x} thin films from reaction of WCl_6 with O-containing solvents and their photochromic and electrochromic properties. Chem. Mater. 17 (6), 1583–1590. https://doi.org/10.1021/cm0403816.
Braslavsky, S.E., 2007. Glossary of terms used in photochemistry. Pure Appl. Chem. 79 (3), 293–465. https://doi.org/10.1351/pac2007 79030293. third ed.
Bhyuiyan, M.M.H., Ueda, T., Ikegami, T., Ebihara, K., 2006. Gas sensing properties of metal doped WO_3 thin film sensors prepared by pulsed laser deposition and DC sputtering process. Jpn. J. Appl. Phys. 45 (1), 8469–8472.
Cao, Y., Cao, Y., Yu, Y., Zhang, P., Zhang, L., He, T., 2013. An enhanced visible-light photocatalytic activity of TiO_2 by nitrogen and nickel-chlorine modification. Separ. Purif. Technol. 104, 256–262.
Chang, X., Sun, S., Xu, X., Li, Z., 2011. Synthesis of transition metal-doped tungsten oxide nanostructures and their optical properties. Artic. Mater. Lett. 65 (11), 1710–1712.
Chauhan, R.P.S., Gupta, C., Prakash, D., 2012. Methodological advancements in green nanotechnology and their applications in biological synthesis of herbal nanoparticles. Int. J. Bioassays 1 (7), 6–10.
Dalrymple, O.K., Yeh, D.H., Trotz, M.A., 2007. Removing pharmaceuticals and endocrine-disrupting compounds from wastewater by photocatalysis. Rev. J. Chem. Technol. Biotechnol. 82, 121–134.
Dwivedi, A.D., Gopal, K., 2010. Biosynthesis of silver and gold nanoparticles using *Chenopodium* album leaf extract. Colloids Surf., A 369, 27–33.
FEPA, 1991. Federal Environment Protection Agency. Guideline and Standards for Environmental Pollution in Nigeria. FEPA, Nigeria.
Fonzo, F.D., Bailini, A., Russo, V., Baserga, A.A., Cattaneo, A., Beghi, M.G., Ossi, P.M., Casari, C.S., Bassi, A.L., Bottani, C.E., 2006. Synthesis and characterization of tungsten and tungsten oxide nanostructured films. Catal. Today 116 (1), 69–73.
Ghaly, A.E., Ananthashankar, R., Alhattab, M., Ramakrishnan, V.V., 2014. Production, characterization and treatment of textile effluents: a critical review. J. Chem. Eng. Process Technol. 5 (182), 8–16. https://doi.org/10.4172/2157-7048.1000182.
Gonzalez-Ortega, J.A., Perea, N., Hireta, G.A., 2006. White light emission from Y2SiO5: Ce, Tb films excited by electroluminescence. Opt. Mater. 29 (1), 47–50. https://doi.org/10.1016/j.optmat.2006.03.007.
Gupta, V.K., Khamparia, S., Tyagi, I., Jaspal, D., Malviya, A., 2015. Decolorization of mixture of dyes: *a critical review*. Glob. J. Environ. Sci. Manag. 1 (1), 71–94.
Hariharan, V., Radhakrishnan, S., Parthibavarman, M., Dhilipkumar, R., Sekar, C., 2011. Synthesis of polyethylene glycol (PEG) assisted tungsten oxide (WO_3) nanoparticles for L-dopa bio-sensing applications. Talanta 85 (4), 2166–2174.
Harshulkhan, S.M., Nagarajan, M., Janaki, K., Velraj, G., Ganapthy, R.S., 2016. Effect of Ag doping on structural, optical and photocatalytic activity of tungsten oxide (WO_3) nanoparticles. J. Mater. Sci. Mater. Electron. 27 (5), 4744–4751.
He, Y., Cai, J., Li, T., Wu, Y., Lin, H., Zhao, L., Luo, M., 2013. Efficient degradation of RhB over $GdVO_4$/g-C_3N_4 composites under visible-light irradiation. Chem. Eng. J. 216, 721–730.
Ibhadon, A.O., Fitzpatrick, P., 2013. Heterogeneous photocatalysis: recent advances and applications. Catalysts 3, 189–218.
Jin, S.Q., Liu, G.H., 2016. Preparation and photocatalytic activity of fluorine doped WO_3 under UV and visible light. Digest J. Nanomater. Biostruct. 4 (11), 1179–1188.
Komaba, S., Kumagai, N., Kato, K., Yashiro, H., 2000. Hydrothermal synthesis of hexagonal tungsten trioxide from Li_2WO_4 solution and electrochemical lithium intercalation into the oxide. Solid State Ionics (135), 193–197.
Li, X., Xu, H., Chen, Z.S., Chen, G., 2011. Biosynthesis of nanoparticles by microorganisms and their applications. J. Nanomater. 1–16 [article 270974].
Li, W., Li, J., Wang, X., Chen, Q., 2012. Preparation and water-splitting photocatalytic behavior of S-doped WO_3. Appl. Surf. Sci. 263, 157–162.
Li, Q.H., Wang, L.M., Chu, D.Q., Yang, X.Z., Zhang, Z.Y., 2014. Cylindrical stacks and flower-like tungsten oxide microstructures: controllable synthesis and photocatalytic properties. Ceram. Int. 40 (3), 4969–4973.
Liu, Z., Bando, Y., Tang, C., 2003. Synthesis of tungsten oxide nanowires. Chem. Phys. Lett. 372, 179–182.
Liu, H., Peng, T., Ke, D., Peng, Z., Yan, C., 2007. Preparation and photocatalytic activity of dysprosium doped tungsten trioxide nanoparticles. Mater. Chem. Phys. (104), 377–383.
Liu, Y., Li, Y., Li, W., Han, S., Liu, C., 2012. Photoelectrochemical properties and photocatalytic activity of nitrogen-doped nanoporous WO_3 photoelectrodes under visible light. Appl. Surf. Sci. 258 (12), 5038–5045.
Mahan, A.H., Parilla, P.A., Jones, K.M., Dillon, A.C., 2005. Hot-wire chemical vapor

deposition of crystalline tungsten oxide nanoparticles at high density. Chem. Phys. Lett. 413 (1), 88–94.
Morales, A.E., Mora, E.S., Pal, U., 2007. Use of diffuse reflectance spectroscopy for optical characterization of un-supported nanostructures. La Revista Mexicana de Física 53, 18–22.
Mu, W., Xie, X., Li, X., Zhang, R., Yu, Q., Lv, K., Wei, H., Jian, Y., 2015. Characterizations of Nb-dopedWO_3 nanomaterials and their enhanced photocatalytic performance. R. Soc. Chem. 4, 36064–36070.
Neppolian, B., Choi, H.C., Sakthivel, S., Arabindoo, B., Murugesan, V., 2002. Solar/UV-induced photocatalytic degradation of three commercial textile dyes. J. Hazard Mater. 89 (2), 303–317.
Ng, K.H., Minggu, L.J., Kassim, M.B., 2013. Gallium-doped tungsten trioxide thin film photoelectrodes for photoelectrochemical water splitting. Int. J. Hydrog. Energy 38 (22), 9585–9591.
Nguyen, T.A., Jun, T.S., Rashid, M., Kim, Y.S., 2011. Synthesis of mesoporous tungsten oxide nanofibers using the electrospinning method. Mater. Lett. 65 (17–18), 2823–2825.
Ntuli, F., Omoregbe, I., Kuipa, P., Muzenda, E., Belaid, M., 2009. Characterization of effluent from textile wet finishing operations. In: Proceedings of the World Congress on Engineering and Computer Science 1, San Francisco, USA, ISBN:978-988-17012-6-8.
Rao, M.C., Hussain, O.M., 2011. Growth and characterization of vacuum evaporated WO_3 thin films for electrochromic device application. Res. J. Chem. Sci. 1 (17), 92–95.
Rettie, A.J.E., Klavetter, K.C., Lin, J., Dolocan, A., Celio, H., Ishiekwene, A., Bolton, H.L., Pearson, K.N., Hahn, N.T., Mullins, C.B., 2014. Improved visible light harvesting of WO_3 by incorporation of sulfur or iodine: a tale of two impurities. Chem. Mater. 4 (26), 1670–1677.
Sathishkumar, P., Pugazhenthiran, N., Mangalaraja, R.V., Asiri, A.M., Anandan, S., 2013. ZnO supported $CoFe_2O_4$ nanophotocatalysts for the mineralization of Direct Blue 71 in aqueous environments. J. Hazard Mater. 252, 171–179.
Seyama, T., Adachi, K., Yamazaki, S., 2012. Kinetics of photocatalytic degradation of trichloroethylene in aqueous colloidal solutions of TiO_2 and WO_3 nanoparticles. J. Photochem. Photobiol. Chem. 249, 15–20.
Shirvastava, V.S., 2012. Photocatalytic degradation of Methylene blue dye and Chromium metal from wastewater using nanacrystalline TiO_2 semiconductor. Arch. Appl. Sci. Res. 4 (3), 1244–1254.
Sin, J.C., Lam, S.M., Mohamed, A.R., Lee, K.T., 2012. Degrading endocrine disrupting chemicals from wastewater by TiO_2 photocatalysis: a review. Int. J. Photoenergy (2012), 1–23. https://doi.org/10.1155/2012/185159.
Song, X.U., Yang, E., Liu, G., Zhang, Y., Liu, Z.S., Chen, H.F., Wang, Y., 2010. Preparation and photocatalytic activity of Mo-doped WO_3 nanowires. J. Nanoparticle Res. 12 (8), 2813–2819.
Song, H., Li, Y., Lou, Z., Xiao, M., Hu, L., Ye, Z., Zhu, L., 2014. Synthesis of Fe-doped WO_3 nanostructures with high visible-light-driven photocatalytic activities. Appl. Catal. B Environ. 166–167, 112–120.
Supothina, S., Seeharaj, P., Yoriya, S., Sriyudthsak, M., 2007. Synthesis of tungsten oxide nanoparticles by acid precipitation method. Ceram. Int. (33), 931–936.
Supothina, S., Rattanakam, R., Suwan, M., 2013. Effect of precursor morphology on the hydrothermal synthesis of nanostructured potassium tungsten oxide. Microelectron. Eng. 108, 182–186.
Tojo, S., Tachikawa, T., Fujitsuka, M., Majima, T., 2008. Iodine-doped TiO_2 photocatalysts: correlation between band structure and mechanism. J. Phys. Chem. C 112 (38), 14948–14954.
Tokunaga, T., Kawamoto, T., Tanaka, K., Hayashi, Y., Sasaki, K., Kuroda, K., 2012. Growth and structure analysis of tungsten oxide nanorods using environmental TEM. Nanoscale Res. Lett. 7 (1), 85.
United Nation (UN), 2017. International Decade for Action Water for Life, 2005– 2017. Water Scarcity.
Uwidia, I.E., 2011. Prediction of Five-Day Biochemical Oxygen Demand (BODs) Values from More Readily Determinable Pollution Characteristics. PhD Thesis. University of Benin, Benin City.
Uwidia, I.E., Ademoroti, C.M.A., 2012. Correlation of suspended solids (ss) and permanganate value (pv) of domestic sewage from an estate in Warri, Nigeria. Glob. J. Res. Chem. Eng. 12 (1), 32–36.
Wang, J., Khoo, E., Lee, P.S., Ma, J., 2009. Controlled synthesis of WO_3 nanorods and their electrochromic properties in H_2SO_4 electrolyte. J. Phys. Chem. C 113, 9655–9658.
Washizu, E., Yamamoto, A., Abe, Y., Kawamura, M., Sasaki, K., 2003. Optical and electrochromic properties of RF reactively sputtered WO_3 films. Solid State Ionics 165 (1–4), 175–180.
WHO, 2011. World Health Organization, 4thedition1. Guildlines for Drinking Water Quality, Geneva Switzerland. http://apps.whoint/iris/bitsream/10665/44584/1/9789241548151_eng.pdf.
Wicaksana, Y., Liu, S., Scott, J., Amal, R., 2014. Tungsten trioxide as a visible light photocatalyst for volatile organic carbon removal. Molecules 19, 17747–17762. https://doi.org/10.3390/molecules191117747.
Wu, Y., Xing, M., Tian, B., Zhang, J., Chen, F., 2010. Preparation of nitrogen and fluorine co-doped mesoporous TiO_2 microsphere and photodegradation of acid orange 7 under visible light. Chem. Eng. J. 162 (2), 710–717.
WWAP (United Nations World Water Assessment Programme), 2015. The United Nations World Water Development Report 2015: Water for a Sustainable World. UNESCO, Paris.
Zhang, X., Huang, Z.-H., Xu, Y., Kang, F., 2012. Hydrothermal synthesis of iodine-doped Bi_2WO_6 nanoplates with enhanced visible and ultraviolet-induced photocatalytic activities. Int. J. Photoenergy 1–12.